A Comprehensive Study on Optical, Electrical and Photophysical Properties of Nanoscale Semiconductor

Krishnarya Vikram Bansal*1

*1Student, Grade 12th The International School, Bangalore, Karnataka, India.

ABSTRACT

Semiconductors are very interesting and attractive class of material due to its wide applications in electronic, optoelectronic and energy conversion devices. Energy band gap and characteristic features of both valence and conduction bands determine unique and novel electronic and optical properties of semiconductors. The physical properties of semiconductor can be easily tuned by reduction of size to nanometer scale, changing morphology and also by doping with appropriate elements. The research work will be focused on preparation of nano scale semiconductor by colloidal synthesis and characterization of these samples by optical and electrical studies. Photophysical properties of nanocomposite are also studied like H2 generation from water, pollutant dye degradation and carcinogenic Cr(VI) reduction from water under irradiation of solar simulator light. In following section a brief outline of optical and electrical properties in nano scale semiconductors are discussed.

Keywords : Atoms, Semiconductors, Carcinogenic, Nanomaterial, Morphology and Nanoscale

I. INTRODUCTION

Semiconductors materials are widely used elemental components in modern technological accessories. Size reduction in semiconductor crystal is a unique opportunity to tune electronic and optical properties compare to bulk state. The atoms resides at surface of nanomaterial are coordinatively unsaturated hence behave differently from saturated bulk atom. Size reduction to nanoscale limit in modern era is the fascinating and emerging field of science and engineering that are evolving at a very fast pace [1]. The growing demand of size reduction in integrated circuit chip also boosted to fabricate various type of nanostructures. Nanotechnology or Nanoscale science is a new world of scientific domain below 100 nanometer dimension deviate from bulk counterpart. Nanomaterials are exploring in various fields at recent times such as soar cells, smart windows, transparent conducting glasses, gas sensors, biosensors, humidity sensors, ultra violet sensor, nonlinear optical devices,8 catalysis, photocatalytic hydrogen generation, photocatalytic CO_2 reduction, SERS (surface enhance Raman spectroscopy) detection, photonic band gap materials, lasers, magnetic imaging, electrical storage devices, cancer cell detection, photothermal therapy in tumor cell destruction etc. Now in recent aliovalent doped degenerate semiconductor nanocrystals (NCs) are addressed considerable attention for localized surface plasmon resonance (LSPRs) absorption, optical bandgap enhancing, multiple emission centers and high carrier concentration with excellent visible light transparency

[2]. Depending on nanoparticles size, dopant concentration and dopant distribution can be varied to tune plasmon absorption in wide optical spectral range from visible to far-infrared regions. Choice of tuning plasmon band in wide spectral range results in the controlled coupling of the LSPR to other physical signatures or the enhancement of optical signals in the NIR range, sensing application by LSPR tracking, energy production from the NIR plasmon resonance or bio-medical applications in the biological window.

The brilliant physicist Richard Feynman originally used the phrase "nano-technology" in his inspirational speech "There's Plenty of Room at the Bottom," which he delivered on December 29, 1959, at a meeting of the American Physical Society at Caltech. Nanotechnology, as defined by Professor Norio Taniguchi of Tokyo Science University in 1974, is primarily the processing, separation, consolidation, and deformation of materials by one atom or by one molecule [3]. Dr. K. Eric Drexler, who addressed the technological significance of nanoscale phenomena and devices in speeches and the books The Coming Era of Nanotechnology (1986) and Nanosystems: Molecular Machinery, Manufacturing, and Computation (1988), explored the fundamental concept of nanoscience in the 1980s in much more detail [4]. Early in the 1980s, two significant inventions the development of the scanning tunnelling microscope and the emergence of cluster science boosted interest in nanoscience and nanotechnology (STM).

The atomic force microscope (AFM) was invented in 1986. This was the turning point for the scientists to fabricate miniature structures. Gradually scientists were achieved more miniature structures from micron to nano dimensions. Nanostructures samples are grown by two techniques: "top down" and "bottom up" approach. In "top down" method nanostructures are fabricated from bulk entities without any precious control over atomic level [5]. There are few methods in "top down" method like attrition, ball milling and lithography where no options of uniform particle size formation. Besides this in bottom up approach it is possible to fabricate nanomaterials through atom by atom or molecule by molecule deposition. This gives a precious control over the size, morphology, structure, chemical composition, homogeneity and defects states. Gradual increasing demand in application of nano materials a variety

numbers of technique have been reported in literatures [6]. successful synthesis of nanomaterials in physical routes mainly addressed RF magnetron sputtering, Physical and chemical vapour depositions, metal organic chemical vapor deposition (MOCVD), atomic layer deposition (ALD), ultrasonication etc. Chemically semiconducting and metal nanostructures synthesis can be performed by sol-gel, hydrothermal / solvothermal, single-source precursors, surface-functionalization, spray pyrolysis, ion layer gas reaction (ILGAR) methods. Similarly DNA, Virus and mesoporous materials have been prepared by different biosynthesis and biotemplate processes [7]. However due to limitations over controlled synthesis of vapour and solid-phase approaches are often unsuitable. Thermal decomposition of precursors in solution mode /colloidal technique is the modern efficient wet chemical route for synthesis of monodisperse well crystalline nanoparticles. Inkjet printing, roll-to-roll casting, and spin coating are just a few of the solution-based devices producing tools that may benefit directly from using stable liquid suspensions. Due to their very high throughput and cheap cost of fabrication, these methods are highly sought after in the large-scale device manufacturing industry.

II. NANOPARTICLE: NUCLEATION AND GROWTH

Thermal decomposition method or colloidal technique is an organometallic solution based nanoparticles synthesis protocol discovered at late 1990 decade and developing on. Simple decomposition of organometallic salt such as metal-carbonyl complex, metal-long chain fatty acid salt in a non-polar solvent medium in presence of some capping agent which must contain a binding group (neutral/positive or negatively charged head) at high temperature can create mono disperse nanoparticles of different materials [8].
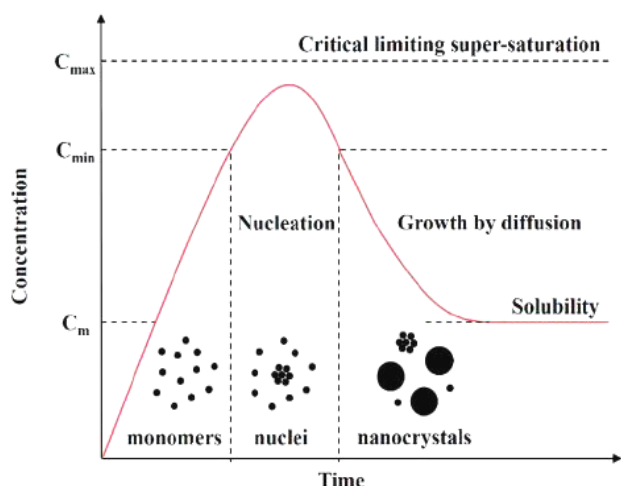
Figure.1: Evolution of monomer concentration vs time according Lamer's theory of burst nucleation.

Colloidal semiconductor nanocrystals (CS-NCs) are produced by controlled synthesis and surface chemical engineering and have the persuasive advantages of cheap cost, wide scale solution processing, and customizable optoelectronic characteristics.

Theory: According to the Lamer model, the fundamental strategies of reaction mechanisms consist of two steps, namely the nucleation stage and the crystal development stage, as illustrated in Figure 1. Following the dispersion of reactant precursors in the appropriate solvents, the chemical reaction between the precursors produces monomers [9]. When the concentration of synthesised monomers approaches supersaturation, they will either aggregate or self-nucleate to form nuclei [10]. The growth process will continue until the monomer concentration falls below the critical limit, as seen in Figure 1, due to the continuous aggregation of monomers on these recently produced nuclei. It should be mentioned here that it may be possible new nuclei formation during growth of nanocrystals, these are result in widening of size distribution.

The theory's underlying premise is that the thermodynamic system seeks to reduce Gibbs free energy or raise entropy. The spherical nanocluster's Gibbs free energy may be written as

$$\Delta G = -\frac{4}{3}\pi r^3 |\Delta G_V| + 4\pi r^2 \gamma \quad (1)$$

where r is the radius, $|\Delta G_V|$ is the difference in the Gibbs free energy per unit volume and γ is the surface energy per unit area i.e. the energy needed to create a surface of unit area. There are two words for Gibss free energy[11]. The first term has a negative expression,

and a typical finding is a reduction in free energy. It refers to a monomer's attachment to the cluster. The second term is a positive word that indicates an unfavourable rise in the energy surface after a monomer's bonding [12]. The rivalry between the loss in volume energy and the rise in surface energy is what causes the change in Gibbs free energy caused by the arrangement of a link between a cluster and a monomer. By equating the first derivative of equation.1. to zero, we get the critical radius of monomer $rc=2\gamma/|\Delta GV|$. If the positive surface energy increases to the higher, then the total system tries towards dissolution and the

growth is unfavorable. Above rc negative energy term survived, growth is favorable phenomena.
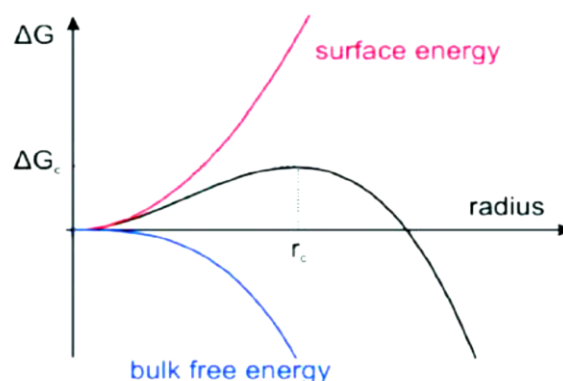

Figure.2: Evolution of the Gibbs free energy of a cluster versus its size (black curve). The evolution of the two terms in the Gibbs free energy equation is also shown: the volume (or bulk) energy (blue curve) and the surface energy (red curve). The critical radius rc and the activation energy ΔGc are also presented.

Figure.2. depicts the evolution of Gibbs free energy of a cluster. In figure ΔGc corresponds to barrier energy at rc. In reaction chamber when the energy barrier is overcome and critical radius is achieved then stable cluster nuclei form in solution [13]. Theses nuclei may commit further growth via heterogeneous nucleation. When nucleation is started nanoparticles formation always try to reduce surface energy. Previously at 1874 Gibbs proposed that the shape of the crystal is depend on minimization of total surface energy *i.e* there should be a option of facet dependency [14]. In 1901 Wulff assumed that surface free energy of a crystal depends on the preferential facet (facet belong to lowest surface energy) orientation.

A. *Wulff Construction Method of Facets*

The simplest case in isotropic phase it turns out as a sphere, but in other case where different complex shape may be evolved due to other low energy facets. An elementary construction method allows us to determine the preferred shape of nanocrystals as developed by Wulff popularized by Wulff construction method [15]. For evolution of low energy facet it is needed to know the energy of a particular facet per unit area in the direction normal to the atomic plane (*hkl*). The corresponding energy roughly proportional to the number of broken bonds on the surface: due to tiny inter atomic distances between atoms on the facets with high coordination factor *i.e* little bit less dangling bonds per unit area result in lowering surface energy with respect to other facet with more dangling bonds [16]. When the energy of particular orientation of facet is known one can plot the plane normal to (hkl) at a distance *c.γhkl* (where *C* is a constant) of the origin of crystal symmetry axes. The same method applied for all other planes. From here we get information about nanocrystals shape. Figure.3. depicted an example of the Wulff construction for a orthorhombic structure , where *γ100 = γ110 = 1/2γ010* except all other planes have higher surface energy [17]. Here the equilibrium shape in this structure is rod-like prism, which is experimentally proved aragonite CaCO3. Shape of nano particle not only depends on thermodynamic equilibrium but also there have kinetic effects on effect. Indeed, depending on growth rate nanoparticles can be arrested by ligands in intermediate state where local energy is minimum [18]. In supersaturated condition nucleation holds for a fraction of a microsecond to a few milliseconds. Here may be an option for reorganization of atoms after nucleation though it is not sufficient for the structure to locate the absolute energy minimum, thus the nanoparticles are arrested in a metastable condition and lead to the final shape of nanoparticles. Hence the growth sequence may be dramatically altered by influence of ligands. Indeed ligands can capable to cap specific facets, slowing down the growth of the passivated facets compared to other one [19]. If the growth in same crystallographic directions is hindered result in rod or plate like morphologies can obtained. This is called chemical positioning. The character of ligand is very much important: it can be organic or inorganic and its tiny change leads to a complete

different result. For evidence from previous literature wurtzite CdS or CdSe/CdS nanocrystals can be synthesized with rod, tetrapod, or plate like shapes [20] depending on ligand and the synthesis conditions. Use of phosphonic acid as ligand hindered the nanocrystals growth perpendicular to the wurtzite C axis, result in rod shaped morphology [21]. In as synthesized nanoparticles synthesis polar headed ligand tightly binds nanoparticle surface by electrostatic interaction lead to the colloidal stability of particle. At later section a details discussion of surfactant in nanocrystal synthesis are presented.
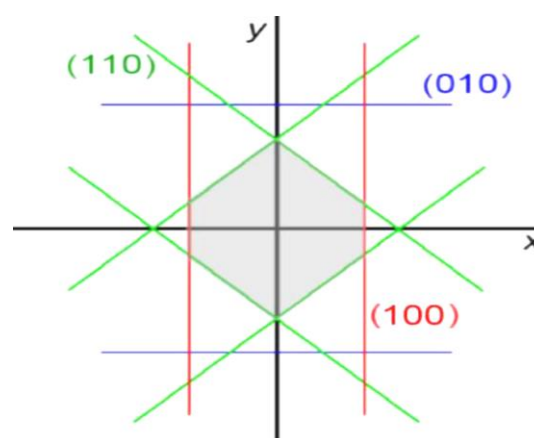

Figure.3: Example of Wulff construction for an orthorhombic structure. The equilibrium shape is shown in gray and comprised in the lines corresponding to the low-energy facets.
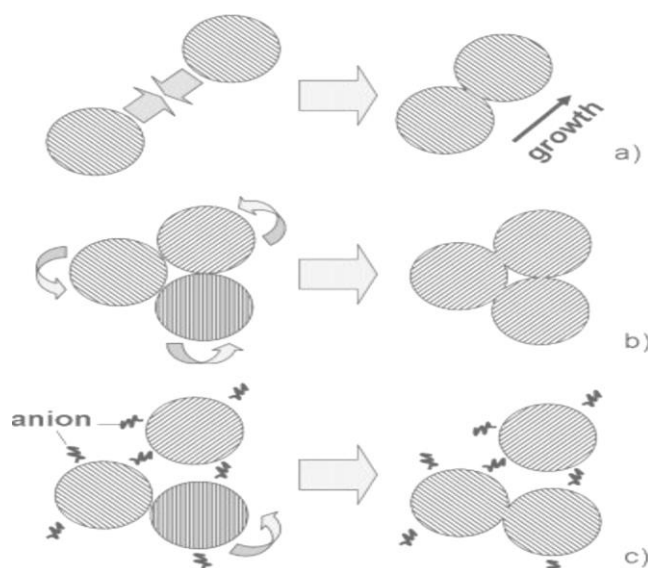

Figure.4: (a) Coalescence in a well-dispersed system: the event is caused by an effective collision, and the growth direction is determined statistically.(b) Coalescence in an agglomerated system: the event can occur at any point of the particles' surfaces provided the crystallographic conditions are favorable. (c) Coalescence in an

agglomerated system with dispersed organic anions acting as steric agents: the event depends on the contact between particles.

B. Oriented Attachment Process

Frequently when the nuclei are present in solution they can grow via addition of precursor or by self assemblies among themselves. In 1998 Penn and Banfield first reported the anisotropic growth of TiO2 nanoparticle via oriented attachment (OA) process [22]. In this type orientation same types of crystallographic planes are coalescence or fused to each other to minimize surface energy or to decrease of number of unsatisfied surface bonds. Apart from this OA can occur between nano particles belongs to different structures. The only criterion is two daughter nanocrystals have facet with similar symmetry [23]. Main steps of OA are depicted in Figure.4. The nanocrystals must first disperse and come into close proximity to one another. The direction of the NCs is hence not necessarily coherent, and OA is prevented since the diffusion may be assimilated to a random walk process controlled by Brownian motion. In order for the NC to align with its neighbour and reduce the grain–grain boundary energy, the NPs must rotate. Finally, a new crystal is produced by the attachment of NCs and the desorption of ligands at the interface. The diffusion of NCs seems to be the limiting stage, according to kinetic studies.

C. Hot Injection and Non Injection Method

To achieve the good size distribution in nanoparticles synthesis one of the most promising method is thermal decomposition method. For a balanced size distribution, the following issues are crucial: Precursor content and reactivity, solvent, surfactant, and pH effects, as well as (a) reaction temperature and time (b) injection temperature of the reactant in the event of a hot injection procedure. Work with narrow size distribution is quite difficult [24]. A tight relationship exists between size distribution and the kinetics of the nucleation and growth processes. It is conceivable for nucleation and growth to proceed independently or simultaneously during the response time [25]. This causes a poor size distribution because to the contemporaneity of the nucleation and growth mechanisms. A successful strategy to achieve a restricted size distribution is to separate nucleation from growth. When using this process, precursors are often injected into the solvents at high temperatures, which is followed by a drop in reaction temperature to separate nucleation and growth (hot injection method). Murray and colleagues used this technique for the first time in 1993 to synthesise Cadmium chalcogenide nanocrystals [26]. The hot injection method has already extended to synthesized of metal oxide nanocrystals. In 1999 this method was first adapted by [4]. for the purpose of TiO2 nanocrystal synthesis. Here rapid injection of titanium alkoxide in hot precursor solution holding TiCl4, Trioctyl phosphine oxide (TOPO) and heptadecan , followed by at a constant temperature at 300° C for 5 minutes produce spherical anatase nanocrystals bellow 10 nm. The hot injection method also reported for other metal oxide in different literature [27]. For ZnO nanocrystals injecting sodium hydrochloride into the ethanolic solution of zinc acetate at 80°C, for CeO2 injecting cerium benzoylacetonate solution into the OLAM (Oleylamine) solvent at 250°C, for ZrO2 (injecting zirconium(IV) isopropoxide into a mixture of ZrCl4, TOPO and heptadecane at over 300°C, and for WO3 injecting tungsten(V) ethoxide into a mixture containing oleic acid (OLAC) and trioctylamine at 315°C .

Unlike hot injection method non injection can be a good option of nanocrystals synthesis if nucleation and growth is controlled by slowly heating up the solution in presence of required precursors. It is necessary precursors have negligible reactivity at low temperature but have proper reactivity at elevated temperatures [28]. Gradually when the solution is heated up to a certain temperature, a burst of nucleation is happened followed by growth mechanism. Compared to hot injection method this method is far simpler for avoiding injection procedure at particular temperature. For example in 2005 Cao and co-workers synthesized CdSe and CdTe nanocrystals in good size distribution by this method. In this research work both non injection method and hot injection method are applied in synthesis of ZnO, TiO2 and CdO nanocrystals.

D. Role of Surfactant in Thermal decomposition Method

It is very genuine fact that the surfactant has a crucial role in controlling the shape, size, nucleation, growth, and decomposition of organometallic precursors. The surfactant sometimes acts as an „activating agent‟. Normally the decomposition of metal oleate or stearate occurs at much lower temperature in presence of surfactant than their pure stage [29]. In situ formed

complex between metal-carboxylate and surfactant plays a significant role for nucleation of oxide nanocrystals, shape and often stabilizing a particular facet. In colloidal oxide nanocrystal synthesis process, long chain saturated or unsaturated amine (Oleylamine, octadecylamine, dodecylamine, hexadecylamine, Tri-octyl amine), long chain mono or di-alcohol (1-octadecanol, decanol, hexadecyl- 1,2-diol), Trioctyl phosphine oxide (TOPO), Trioctyl phosphine, many saturated and unsaturated fatty acid (stearic acid, palmetic acid, oleic acid etc) etc. are widely used as surfactant and activating agent.
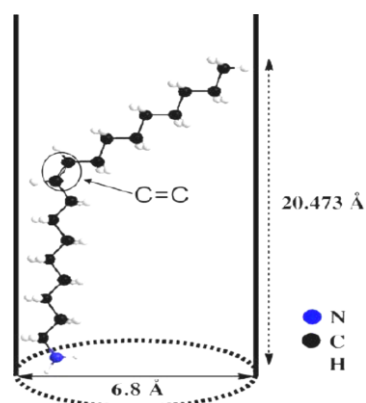

Figure.5: Chemical structure of oleylamine

Oleylamine (OLAM) is an attractive and broadly used surfactant in colloidal nanocrystals synthesis. It acts as activating agent, capping agent, reducing agent at elevated temperature as well as solvent. Figure.5. shows the chemical structure of oleylamine containing a double bond which is often involved in co-ordination with metal ion in solution or in crystalline nanoparticles and a primary amine group which is able to do a nucleophilic attack at electrophillic centre such as carbonyl group [30]. This molecule has a boiling point above 340 °C and below which nucleation of most of oxide nanocrystals takes place.
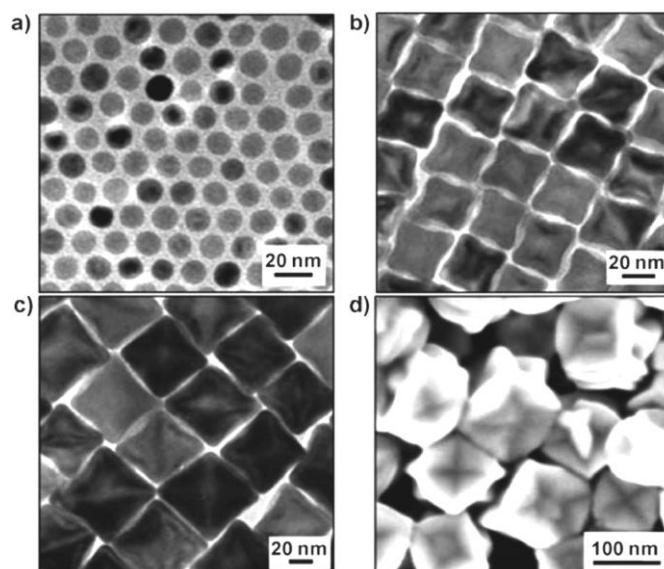

Figure.6: TEM images of different shaped FeO nanocrystals. Relative amount of oleic acid and OLAM determined facet stabilization of the final product

In instance, the generated nanoparticles' shape and crystallinity might vary dramatically even though octadecylamine and OLAM have identical basicity and affinities to metals thanks to their NH2 functional groups [31]. As an example, consider the creation of Au decahedra in the presence of OLAM or octadecylamine (ODA), where it was postulated that ODA's absence of a C=C bond would restrict its coordination with gold chloride (AuCl), leading to altered geometries. Cobalt acetylacetonate [Co(acac)$_3$] was used as a precursor, and OLAM was effectively used in a "triple role" (solvent, surfactant, and reductant) in the production of hexagonal and cubic CoO nanocrystals [32]. The oxygen in CoO is thought to have come from the precursor's acetylacetonate ligand given that the reactions took place in an inert environment. Fe(acac)3 underwent reductive breakdown in an oleic acid/OLAM combination to produce size- and shape-controlled FeO nanoparticles (Figure.6). It was suggested that the final morphology of the particles was determined by the differential in binding between oleate and OLAM on the crystal surfaces [33]. The generation of -Fe$_2$O$_3$ tetrapods using a ternary surfactant combination was explained using the same justification (Oleic acid, OLAM, and hexadecanediol). In a simple heating approach employing iron(III) acetylacetonate as a metal source, Fe3O4 (magnetite) nanocrystals in the range of 7–10 nm were also generated using OLAM as a reducing agent, stabiliser, and cosolvent with benzyl ether. Achieving the right ratios of OLAM, oleic acid, and

hexadecanediol produced Fe_3O_4 nanoparticles that were around 4 nm in size and easily formed self-assembled monolayers and multilayers when hexane was evaporated. Other ferrite nanocrystals with the general formula MFe_2O_4 (M = Fe, Co, Mn) were also synthesised using this method. It was shown that the creation of the desired particles required the combined use of oleic acid and OLAM, while oleic acid alone would result in a viscous red-brown product that was challenging to purify and describe [34]. However, OLAM alone only produced a very little amount of iron oxide nanoparticles. Using surfactants with various hydrocarbon structures, such as OLAM on the one hand and adamantaneamine, adamantanecarboxylic acid, and trioctylamine on the other, star-like cubes and flower-like magnetite nanoparticles were created by the pyrolysis process [35]. The linear structure of OLAM was thought to affect the particle development mode by attacking the electropositive carbonyl carbon of an intermediate iron complex more readily than the bulky adamantyl groups of adamantaneamine (or the comparable bulky groups of trioctylamine). Additionally, it has been shown that the molar ratio of OLAM to iron oleate is essential for the development of octahedral ferromagnetic Fe_3O_4 NPs.

On the other hand, a successful aminolytic reaction between zinc carboxylates and OLAM in coordinating or noncoordinating solvents led to the production of ZnO nanostructures in a variety of morphologies, including nanorods, nanotetrahedrons, and nanosquamas. Depending on the form and severity of their structural flaws, these nanostructures revealed intriguing optical characteristics such as acute band-edge emission or wide deep-trap emission [36].

Long chain saturated alcohol is another important group of surfactants which are widely used in colloidal nanocrystal synthesis. The activity of R-OH is quite similar with the amines. Nucleophilic OH group can attack the carbonyl centre of metal fatty acid complex easily but at much slower rate than the amine groups. The alcoholysis synthesis procedure has been studied by mainly Xiogang Peng and his co-workers [37]. They studied in details of synthesis of ZnO and In2O3 nanoparticles and effect of side reaction in nanocrystal morphology. This synthesis procedure with the variation of synthetic condition widely studied by other groups and us also. The synthetic procedure is found to be effective for doping and generation of plasmon in aliovalent doped transparent conducting oxide.

III. NANOCOMPOSITE

Due to its capacity for the direct exploitation of solar energy in the creation of solar fuels such as hydrogen and hydrocarbon fuels as well as for the degradation of different pollutants, semiconductor-based photo catalysis is attracting a lot of interest. Solar energy driven photo-catalyst has potential to initiate or accelerated specific oxidation and reduction (redox) reaction [38]. Under irradiation of solar light electron and hole pair are generated in photo-catalyst. The major drawbacks of these kind of catalysis are the short lifetime of photo generated electron hole pair and limited visible-light absorption [39]. To overcome these serious drawbacks the most widely used strategy is to develop photocatalytic nanocomposite. Different types of nanocomposites are fabricated between semiconductor-semiconductor, semiconductor–metal, semiconductor–carbon group and the multi component hetero junction. Typically in nanocomposite different semiconductors with unequal band structure commit to band alignment or band bending.

E. Band Position of Composite

Band offset position of different semiconductor and metal nanoparticles in composite system leads to different types hetero junction conventionally a straddling gap (type-I), staggered gap (type-II), broken gap (type-III) and more promising Z scheme type. In type-I hetero photocatalyst under excitation of light energy electrons and holes are accumulated at the CB and VB of semiconductor B (Figure.7a). The major inaccuracy of this type composite, both electron and hole reside at same semiconductor results in short life time of exciton pair, hence the redox potential energy is reduced in this type catalyst [40]. For type II catalyst system (Figure.7b) the CB and the VB levels of semiconductor A are higher than the corresponding levels of the other semiconductor B. Excitation energy higher than band gap potential result in electron transfer from A to B and holes are migrated from B to A. As the exciton pair resides in different semiconductor here is a chance for enhancement of lifetime in electron hole pair. Enhancement in lifetime triggered the redox reduction potential energy.
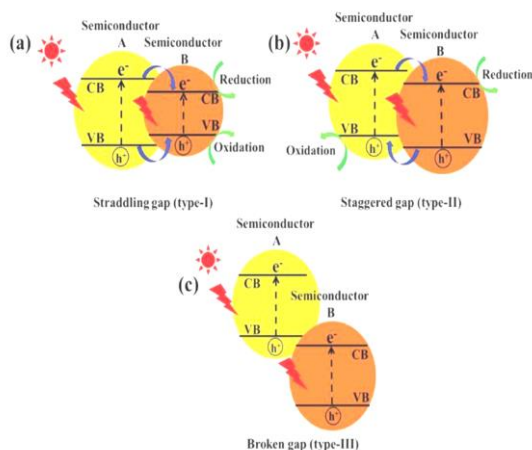
Figure.7: Schematic presentation of the three different types of separation of electron– hole pairs in the case of conventional light-responsive heterojunction/nanocomoposite photocatalysts: a) type-I, b) type-II, and c) type-III heterojunctions.

Hence type II composite is more favorable than type-I. The architecture of type-III heterojunction (Figure.7c) photocatalyst is likewise type-II composite where the staggered gap become so extreme that the bandgap bending is unfavourable [41]. Hence exciton pair separation becomes hard. Because of its suitable structure for the spatial separation of electron-hole pairs in the conventional heterojunction used in the aforementioned conventional nanocomposite, type-II heterojunction is clearly the most effective conventional heterojunction to be used for enhancing photocatalytic activity. Previous literature of different type-II composites are such as SnO2/TiO2, BiVO4/CeO2, ZnO/CdS, BiVO4/WO3, g-C3N4–WO3. In order to enhance the redox reaction efficiency noble metal nanoparticle are decorated on the surfaces of composite. Since semiconductor-metal nanocomposites show a change in the Fermi level to greater negative potentials, they have been exploited as photocatalysts extensively [42]. Such a change in the Fermi level improves the composite system's energetics and increases the effectiveness of the interfacial charge-transfer mechanism. Although type-II nanocomposite may separate electron hole pairs when excited, the ultrafast electron-hole recombination rate in semiconductor prevents the boost in electron-hole separation across a type-II heterojunction that is required [43].
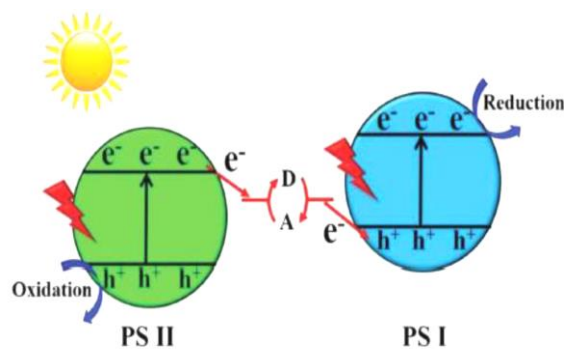

Figure.8: Schematic illustration of electron–hole separation on the conventional Z-scheme photocatalytic system under light irradiation.

Since from the beginning a array of different types of nanocomposite scheme are discussed, there are still remaining some inefficiency such as limited region of visible light photo absorption, inaccuracy in enhancing electron–hole separation, inadequate redox potential energy to drive the redox reaction. In 1979 Bard Z-scheme photo catalyst was proposed to handle the above mentioned problems [44]. Conventional Z scheme photocatalyst system holds two different semiconductor: photocatalyst I (PS I) , photocatalyst II (PS II) and an acceptor/donor (A/D) pair(Figure.8). During photo catalysis photo generated electrons are migrated from CB of PS II to VB of PS I via an A/D pair as shown in Figure.8, via following redox reactions:

$$A + e^- \rightarrow D$$

$$D + h^+ \rightarrow A$$
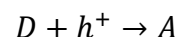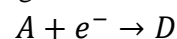
Here, A is converted into D by a reaction with photogenerated electrons from PS II's CB. The photogenerated holes from the VB then oxidise the D into A. As a result, electron-hole pairs spatially separate on PS I, which has a larger reduction potential, and congregate on PS II, which has a higher oxidation potential [45]. This allows for the achievement of the best possible redox ability. A direct Z-scheme (Figure.9) approach for photocatalysis, which combines two distinct semiconductors without the need of an electron mediator, was suggested by J. G. Yu in 2013. With the exception of the system's lack of need for rare and costly electron mediators, the fundamental process is the same as that of a typical Z-scheme.
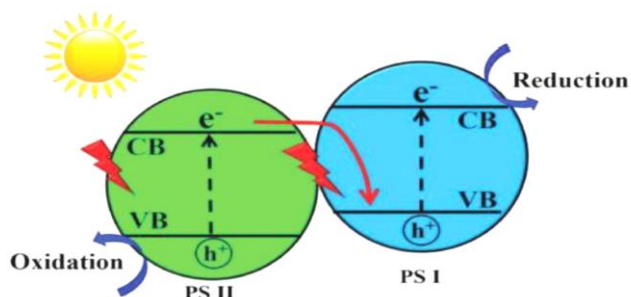
Figure.9: Schematic presentation of electron-hole separation in direct Z-scheme system.

Due to the electrostatic attraction between electrons and holes, the direct Z-scheme heterojunction photocatalyst has a physical advantage over type-II heterojunction photocatalyst in terms of charge transfer [46]. Due to the electrostatic attraction between the electrons and the holes in this situation, the migration of photogenerated electrons from the CB of the PS II to the photogenerated hole-rich VB of the PS I is made simpler. The electrostatic repulsion between electrons makes it difficult for photogenerated electrons to migrate from the CB of semiconductor A to the photogenerated electron-rich CB of semiconductor B in reverse for traditional type-II heterojunction photocatalysts. Previous literature among different material like CdS–WO3, Fe2O3-FeS2, g-C3N4‑TiO2, Ag2CrO4-graphene oxide committed Z scheme pathway in photocatalysis.

IV. SURFACE PLASMON

Surface plasmon resonance (SPR) exploits the coherent electron oscillations that are driven at the frequency of the incident electromagnetic field. Electric component of electromagnetic wave vector excites free electrons to have collective oscillation shown in Figure.10. Collective oscillation results in propagation of electromagnetic surface mode at the interface of metal and surrounding dielectric medium [47]. Surface plasmon resonance addresses couplings of electromagnetic field to the kinetic motion of free charge carriers. Indeed the challenge is plasmonic propagation loss [48].
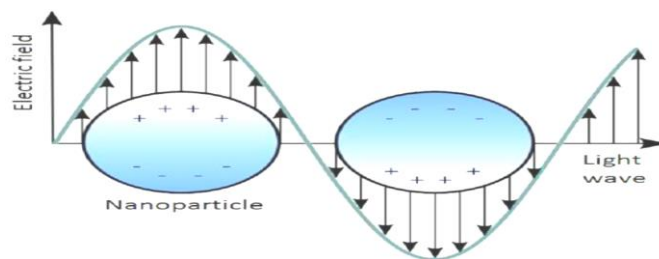

Figure.10: Schematic presentation of the collective oscillation of electrons in metal nanoparticles by excitation of electromagnetic wave.
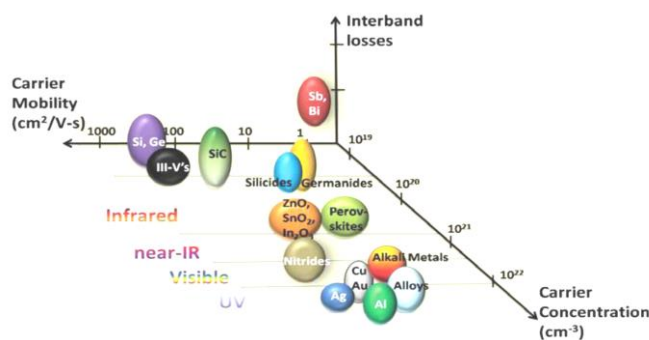

Figure.11: Conclude oxide semiconductor maintain optimum carrier concentration, mitigation loss and carrier mobility.

While presence of negative real part of permittivity in noble metal causes sub wavelength confinement and also have significant large imaginary component of permittivity results in long range plasmonic propagation loss. So it is needed a material which allows sub wavelength optical confinement and loss mitigation simultaneously. Figure.11. demonstrates the classification of materials on the basis of two important parameters that determine the optical properties of conducting materials: the carrier density and carrier mobility [49]. Higher carrier nobilities interpret to lower material losses. From Figure.11. it is convenient that degenerately doped semiconductors are best conductive plasmonic material.

Different types of chemical doping viz. aliovalent substitution doping in oxide semiconductor (mainly transparent conducting oxide (TCO)), vacancy dopping and interstitial doping results excess charge carrier density. In nanoscale regime surface Plasmon resonance is resulting as localized surface plasmon resonance (LSPR) [50]. Excellent achievement in colloidal synthesis of nano TCO material soundly improves the tunability of LSPR. Excitation of LSPR in nanocrystals (NCs) results in strong optical absorption , scattering and strong electromagnetic near field enhancement around the nanocrystals9 those can be tuned in a wide range of optical spectrum from visible to far infrared

region by tuning dopant concentration, post synthetically treatment via chemical oxidation reduction, electrochemical, and photochemical control. Due to remarkable optical absorption, scattering and strong electromagnetic near field enhancement utilize in molecular-specific imaging and sensing, photo diagnostics, and selective photo thermal therapy.

A. Theory of surface Plasmon

The charge carriers are displaced by incoming electromagnetic energy with respect to the nuclei in noble nano metal. Excitation of LSPR by a coherent electric field creates a resonance at a particular wavelength and results in strong surface plasmon absorption band, intense light scattering and an enhancement of coherent electromagnetic field [51]. SPR can be tuned in doped semiconductor by the variation of aliovant dopant concentration, nanoparticles size, shape and surrounding dielectric medium. Traditional noble metals like gold, silver, and platinum may display LSPR in the visible to near-infrared range. Some TCO materials as a result of noble metals cause plasmon resonance in the NIR and MIR because of decreased quantized plasma energy. Drude-Lorentz theory can quantitatively explain how the free carrier concentration in TCO NCs correlates with the plasmon absorption band energy and intensity. There are two decay paths for the surface plasmon energy. One channel is manifested by scattering-loss spectra and other is absorption band cross section. So the total extinction cross section is sum of scattering cross section (Csca) and absorption cross section (Cabs) can be written as:

$$C_{ext} = C_{abs} + C_{sca} \quad (2)$$

Extinction is totally depended on the polarizibility(α) of the nanoparticles. i.e. it includes the dielectric function of metal.

B. Drude Theory

Drude used the kinetic gas hypothesis to explain the thermal and electrical properties of metals. Since he believed that electrons could easily move between collisions, elastic scattering, and phonons or lattice defects. Arnold Sommerfeld updated Drude's theory in this case and adopted the notion that conduction band electrons alone are responsible for determining electrical and optical characteristics [52]. The Drude-Lorentz-Sommerfeld model now describes how metal

is excited by an external electric field. Conduction electrons' freedom of movement inside the bulk of a metal is used to assess its optical qualities, and interband excitation is a possibility if an electromagnetic wave has a higher energy than the material's band gap. In a real-world situation, the existence of an electric field causes an electron to move, r, which is connected to a metal's dipole moment, er, through the equation μ = er. Here, the positive ion core binds the electron displacement, causing Coulomb attraction to function as a restoring force for the electrons. The cumulative action of every single electron in the conduction band is what is responsible for the macroscopic changes in optical and electrical characteristics. Given that the number of electrons per unit volume, n, determines the macroscopic polarisation, P = nμ. Now the electric displacement D is related to this macroscopic polarization by

$$\mathbf{D}(\mathbf{r}, t) = \varepsilon_0\mathbf{E}(\mathbf{r}, t) + \mathbf{P}(r, t) \quad (3)$$

We also have from electro statistic

$$\mathbf{D} = \varepsilon_0\varepsilon\mathbf{E} \quad (4)$$

Combine equation (3) and (4) by assuming isotropic medium, the dielectric constant can beexpressed as:

$$\varepsilon = 1 + |P| / \varepsilon 0|E| \quad (5)$$

Amount of displacement r and macroscopic polarization P can be found out by solving the equation of motion of the electrons that are perturbed by an external electromagnetic field. While in case of bulk metal damping constant (γ) is proportional to the Fermi velocity v_F and inversely proportional to the bulk mean free path l_∞ $(\gamma = v_F/l_\infty)$. At a starting point we can consider the electric field of an electromagnetic wave travelling in X direction with propagation direction along Z axis. Now we consider that

$$\bar{E}_z = \bar{E}_0\varepsilon^{i\omega t} \quad (6)$$

By applying Drude-Sommerfeld model equation of motion of an electron with mass m_e and charge e is governed by

$$m_e\partial x^2/\partial t^2 + m_e\gamma \, \partial x/\partial t + m_e\omega_0^2 x = -e\bar{E}_0 e^{i\omega t} \quad (7)$$

Where E_0, ω and ω_0 are the amplitude, the frequency of the applied electric field and induced frequency of oscillating electron. The solution of equation (7) is

$$(t) = -e\,\bar{E}_0 e^{i\omega t}/me(\omega_0^2 - \omega^2 - i\gamma\omega) \quad (8)$$

Microscopic dipole moment P is connected to the polarization p with carrier density n in conduction band by

$$P = n.p = -n.e.x \quad (9)$$

By combining equation (5),(6) and (7) leads to

$$\varepsilon(\omega) = 1 + n_e^2/\varepsilon_0 m(\omega_0^2 - \omega^2 - i\gamma\omega) = 1 - n_e^2\,\omega_p^2/\varepsilon_0 m_e$$
$$(\omega_0^2 - \omega^2 - i\gamma\omega) \quad (10)$$

Where

$$\omega_p^2 = n_e^2/\varepsilon_0 m_e \quad (11)$$

ωp is the volume plasma frequency with vacuum permittivity $\varepsilon 0$. In lattice environment scenario it might be change me by m^*, the lattice electron effective mass. Finally the frequency dependent dielectric function can be expressed as:

$$\varepsilon(\omega) = \varepsilon'(\omega) + i\varepsilon''(\omega) = 1 + \omega_p^2(\omega_0^2 - \omega^2)/[(\omega_0^2 - \omega^2)^2$$
$$+\gamma^2\omega^2 + i\omega_p^2\gamma\omega\,[(\omega_0^2 - \omega^2)^2 + \gamma^2\omega^2] \quad (12)$$

In conduction band scattering of electrons with electrons (e-e), lattice defect(e-d) and phonon(e-p) results in damping of collective oscillation. At free electron theory damping constant is depicted by the inverse of the scattering time of the electron:

$$\gamma = \tau^{-1} = \tau_{e-e}^{-1} + \tau_{e-d}^{-1} + \tau_{e-ph}^{-1} \quad (13)$$

For the bulk electron-phonon term is denominating one hence γ should be a constant. In case of small particles due to size reduction surface acts as an additional scatter where mean free path of electrons becomes comparable to the size of particles. In nano dimension these interactions of the conduction electrons with particle surface dominate which result in a reduced effective mean free path of electrons. According to Drude model the damping constant γ can be expressed as in term of particle radius such as :

$$(R) = \gamma_0 + A.v_F/R \quad (14)$$

Where $\gamma 0$ is the bulk damping constant vF is the velocity of the conduction electrons at the Fermi energy, and A includes details of the scattering processes.

C. Mie Theory

Gustave Mie published the first description of the discovery about the light scattering by spherical metal structures within the context of electrodynamics in 1908. By selecting the proper boundary condition and using numerous expansions of the electric and magnetic field, he was able to solve the Maxwell equation while taking into account the particle size and optical material functions of the particle and the surrounding medium as input factors.

It is possible by Mie theory to get an understanding of light scattering by structures with other regular shapes, such as cylinders with arbitrary radius and ellipsoids with any size. Now for the particles much smaller than the incoming electromagnetic effect i.e., $R \ll \lambda$ then cross-sections for scattering, extinction and absorption can be expressed as:

$$C_{ext}^{Mie} = 2\pi/k^2 \sum(2n + 1)\,R(a_L + b_L) \quad (15)$$

$$C_{Sc}^{Mie} = 2\pi/k^2 \sum(2n + 1)\,\{|aL|^2 + |bL|^2\} \quad (16)$$

$$C_{abs}^{Mie} = C_{ext}^{Mie} - C_{Sc}^{Mie} \quad (17)$$

Where $k = 2\pi/\lambda$ and a_L and b_L are the scattering cross section coefficient. These are the particle size parameter (α) depended index which are governed by

$$\alpha = 2\pi r/\lambda \quad (18)$$

$$a_L = [m\psi(m\alpha)\,\psi'(\alpha) - \psi L'(m\alpha)\,\psi_L(\alpha)]/[m\psi(m\alpha)$$
$$n_L'(\alpha) - \psi_L'(m\alpha)\,n_L(\alpha)] \quad (19)$$

$$b_L = [\psi(m\alpha)\,\psi'(\alpha) - m\psi L'(m\alpha)\,\psi_L(\alpha)]/[\psi(m\alpha)\,n_L'$$
$$(\alpha) - \psi_L'(m\alpha)\,n_L(\alpha)] \quad (20)$$

Where ψ_L and n_L are represents the Riccati-Bessel functions and prime indicates the first derivative of function. Here $m = n/n_m$, n is a complex number as metallic particle have absorbing and its refractive index nm is the real refractive index of liquid surrounding medium. Here L is the summation index of admitted the spherical multipole excitations in the particle. In case of small particles for dipole scattering resonance, only the term $l=1$ is applied in Mie theory and other higher order term $l = 2$ to quadrupolar fields and so on are neglected. So in dipolar field approximation C_{ext}^{Mie} for spherical particle simplified as:

$$C_{ext}^{Mie} = \{[18\pi V\varepsilon_m^{3/2}]/\}\,[\varepsilon''(\omega)/\{(\varepsilon'(\omega) + 2\varepsilon m)^2 + \varepsilon''^2(\omega)\}] \quad (21)$$

εm is the dielectric constant of surrounding medium , ε_ω is the dielectric constant of spherical particle. V is the volume of spherical particle. C_{ext} has admitted a resonance when $(\varepsilon'(\omega) + 2\varepsilon m)^2 + \varepsilon''^2\omega$ is minimum. When $(\varepsilon''(\omega))$ is also very small then at resonance.

$$\varepsilon'(\omega) = -2\varepsilon_m \quad (22)$$

D. Influence of dopant concentration on LSPR

Charge carriers are seen as virtually free, non-interacting "quasi-particles" in the traditional Drude model, only interacting with lattice nuclei, vacancies, and dopant ions by immediate impact. This is the fundamental concept that links the free carrier density with SPR absorption. As can be shown in Figure, the charge carrier density in the NCs is related to the LSPR frequency. 12. The Drude approximation of the dielectric function of a material with free charge carriers is shown in equation (11). In equation (11), meff is the effective mass of the charge carriers, p is the bulk plasmon frequency, is a damping frequency, n is the density of free charge carriers, e is the charge of the electron, and 0 is the vacuum permittivity (electrons or holes). Free carriers provide a large LSPR absorption peak in the IR to mid-IR region in alliovalent doped TCO materials. Using the LSPR absorption peak and the Drude theory, one may correlate the quantity of doping in the pure sample with the concentration of free carriers in the doped TCO material. However, the application of this straightforward methodology may be limited by issues like the polydisparity of NCs and non-uniform elements distribution. Here Figure.12. depicts the plasmon absorption band position in energy scale with carrier concentration.
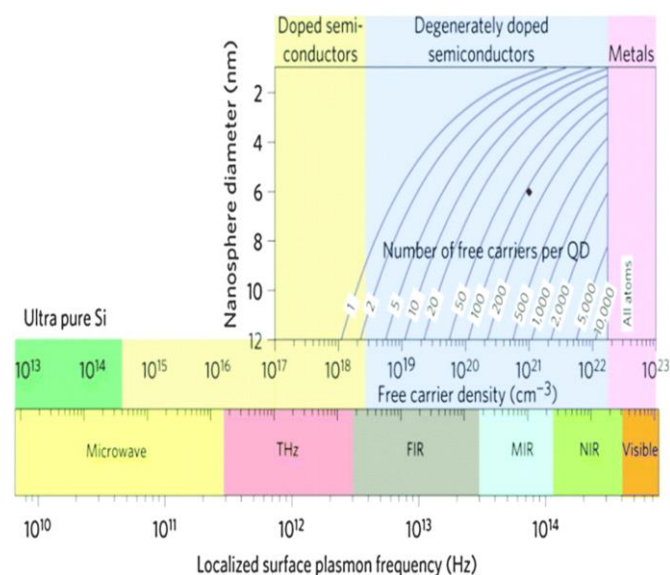

Figure.12: LSPR frequency is associated with the charge carrier density in the NCs.

E. Influence of nanoparticle size on the LSPR

Mie's theory provides the total extinction coefficient of tiny metallic particles (equation 21). Only the dipole term is believed to contribute to the absorption for nanoparticles considerably smaller than the wavelength of the absorbed light (approximately 25 nm for gold particles) (dipole approximation). In quasi-static regime where incoming light wavelength much larger than particle size ($R << \lambda$) i.e electron-surface scattering becomes important. The extinction cross section in Mie theory becomes independent of the particle volume, is contradictory with observations found experimentally for small metallic nanoparticles. Since the mean free route of the conduction electron has a higher mean free path when the particle size is smaller, electron scattering at the nanoparticle surface plays a greater role in such tiny particles. In this situation, as particle size decreases, plasmon resonance will expand and move to the red. According to equation 14 of the Drude free electron model, the plasmon resonance bandwidth in this limit is inversely proportional to the particle radius. Hence carriers are scattered elastically from surfaces rapidly, results in incoherence between scattered waves. *S. Link et al.* shown size dependence of the plasmon absorption band as depicted in Figure.13.
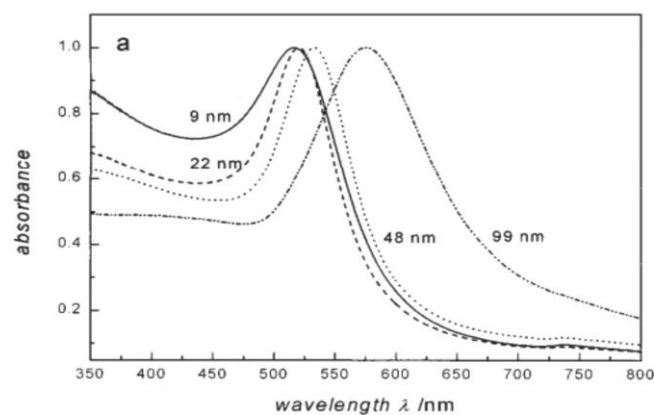

Figure.13: Size effects on the LSPR absorption in spherical gold nanoparticles. The UV-vis absorption spectra of colloidal solutions of gold nanoparticles with diameters varying in between 9 and 99 nm reveal that the absorption maximum red-shifts with increasing particle size.

F. Solvent effect on the LSPR absorption peak

Equation governs the relationship between the dielectric function of the material and the refractive index of the surrounding medium (22). It is proven by equation (22) that the plasmon resonance is dependent on the

surrounding medium's refractive index n ($n^2 = \varepsilon$ m). The plasmon frequency decreases as the dielectric constant gradually rises because the Columbic restoring force of the electron cloud of nanoparticles decreases. The experimentally determined LSPR absorption peak for solvent change is shown in Figure 14. As the solvent's refractive index rises, the LSPR absorption peak is seen to move to the red. Refractive index sensitivity may beneficial for biosensing applications.
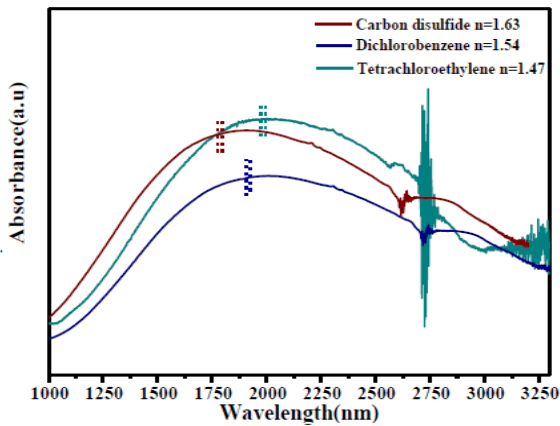

Figure.14: Red-shift of LSPR with increased refractive index.

G. Shape dependency on LSPR absorption

The complicated dielectric function of the material, the surrounding medium (m), and the size and form of the nanoparticles all affect the LSPR absorption wavelength.
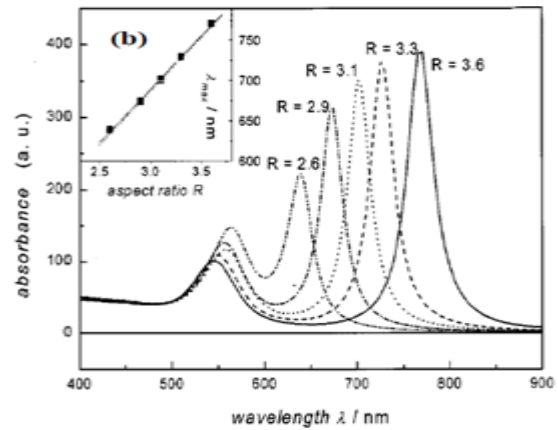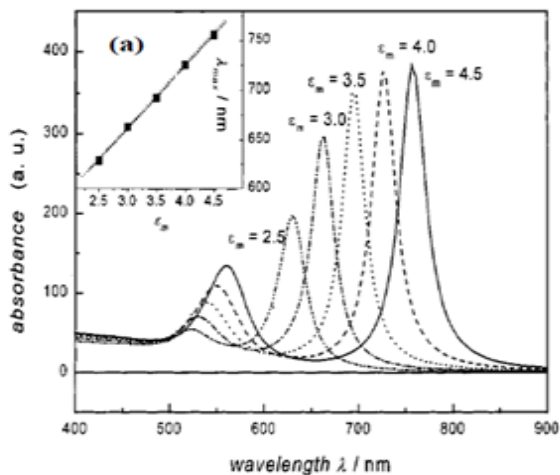

Figure.15: Using eq. 23, (a) calculated the absorption spectra of long ellipsoids whose medium dielectric constant m varied. A fixed aspect ratio of 3.3 was used. The maximum of the longitudinal plasmon band, estimated from the predicted spectra as a function of the medium dielectric constant, is shown in the inset. (b) Equation 26 was used to calculate the absorption spectra of extended ellipsoids with various aspect ratios R. The value of the medium's dielectric constant was set at 4. The maximum of the longitudinal plasmon band as derived from the computed spectra is shown as a function of aspect ratio in the inset.

Anisotropy that is shape dependant significantly affects the LSPR absorption pattern. Since spherical particles have strong symmetry, the excitation of the LSPR in the Mie approximation is independent of the polarisation of excitation. According to R. Gans, the Mie theory may be expanded in the quasi-static regime, where R , by combining the depolarization factors for the particle's three axis in order to account for the contribution of the light polarisation in various modes for the axes of the spectrum. Nanoparticles with variable forms need a computational technique for solving Maxwell's equations using numerical tools, such as the discrete dipole approximation, boundary element method, and finite difference in the time domain method (FDTD) (DDA).

However, electromagnetic wave polarisation plays a great significance for regular structures like nanorods since there are two primary directions of collective oscillation that can be determined, such as parallel to the main axis of the rod or perpendicular to it. The extinction spectrum of previously published gold nanorods revealed two bands, corresponding to oscillations longitudinally (L-band) and perpendicularly to the long axis (transverse or T-band) of the nanorod. Now according to Mie Gans modification extinction cross section (*Cect*) represented as:

$$C_{ext}=[2\pi V\varepsilon_m{}^{3/2}]/\,3\lambda\sum(1/Pj^2)\varepsilon''(\omega)/\{(\varepsilon(\omega)+[1-P_J]$$
$$\varepsilon_m/P_J)2+\varepsilon''^2(\omega)\quad(23)$$

Pj are the depolarization factors for the three axes x, y and z for three dimensional system ($j = A$, B, and C of the nanoparticle with $A > B = C$). Depolarization factors are represented as:

$$Px=[1-e^2]/e^2\,[1/2e\{\ln(1+e/1-e)\}-1]$$
$$(24)$$
$$Py=Pz=\{(1-Px)/2\}$$
$$(25)$$

Where e is geometric factor appeared in equation (24) defined as

$$S=(1-1/R^2)^2$$
$$(26)$$

R is the aspect ratio of nanoparticles. From equation (23) it is clear that two distinct perpendicular bands are arise along with the principal long axis band. Multiple plasmonic bands are studied in differ aspect ratio for gold nanoparticles using equation.23. (Figure.15.)

V. BANDGAP VARIATION IN NANOSCALE SEMICONDUCTORS

Physical properties of bulk crystal depends only its chemical composition only. When bulk material is scale down to nanoscale regime results in quantum confinement effect in semiconductor materials. Quantum confinement leads in an increase in the excitonic transition band gap energy and a blue shift in the absorption and luminescence band energy when the size of the material is equivalent to the Bohr exciton radius. There are essentially three types of low-dimensional systems: two-dimensional (2D) systems, which include thin films, layer structures, quantum wells, and superlattices; one-dimensional (1D) systems, which include semiconductor wires and solids in which linear chain-like structures can be recognised. Finally, zero-dimensional (0D) systems, which include clusters, quantum dots (QDs), and colloids. Excitons are constrained in all three spatial dimensions in the case of QDs. Due to the extraordinarily acute density of states (DOS) that QDs have at the nanoscale, they exhibit numerous different electrical behaviours from bulk low-dimensional semiconductors. The DOS ($\rho(E)$) of nanocrystals simultaneously evolves from continuous levels into discrete states as the dimensionality is decreased from 3D to 0D as described by the relationship $\rho(E) = E^{D/2}-1$ where D = dimensionality

and energy is measured from the bottom of the conduction band for electrons and from the top of the valence band for holes. In the three-dimensional system, $\rho(E)$ is a smooth square-root function of energy. In the case of $d = 2$ and $d = 1$, a number of discrete subbands appear due to the quantum confinement effect. A schematic representation of broken symmetry and the functional form of the density of states in 1D, 2D, 3D, and 0D is shown in Figure 16. It is reasonable to handle with the simplest three-dimensional potential well, which is a spherical potential box with infinite deep potential and electrons and holes have isotropic effective masses, in order to reveal the main quantum confinement effect within the framework of the effective mass approximation (EMA). Here, two different forms of confinement come into play: weak confinement and forceful confinement. In this context, Brus provided the first theoretical estimate of the fluctuation in band gap energy via EMA. Electronic interactions between electrons and electron holes in tiny semiconductor crystallites: The Size Dependence of the Lowest Excited Electronic State,". Here size dependent bandgap energy expressed as :

$$E(qd)=E_{bulk}+h^2/8R^2\,(1/m_{e^*}+1/m_{h^*})$$
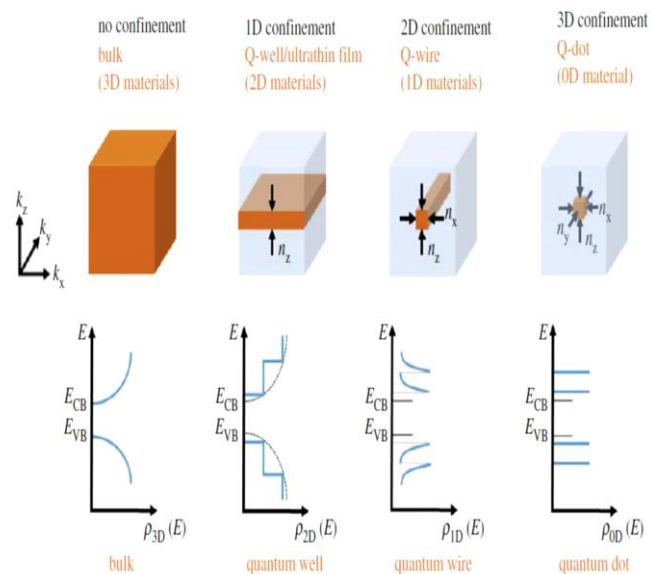$$-1.786e^2/4\pi\varepsilon_0\varepsilon_r R\qquad(27)$$

Figure .16: Schematic illustration of broken symmetry and functional form of the density of states in 1D, 2D and 3D confined materials

Where $Eg(qd)$ = band gap energy of quantum dot; Ebulk = band gap energy of bulk semiconductor; R = radius of quantum dot; me^*= effective mass of excited electron; mh^*= effective mass of excited hole; h = Planck's constant , ε_0 = permittivity of vacuum εr = relative permittivity. the first term on the right side of the equation. The second additive term of the equation, which is represented by the additional energy due to quantum confinement and has an R-2 dependence on the band gap energy, stands for the columbic interaction energy, with the exciton having an R-1 dependency. Equation (27) represents the band gap energy of bulk materials (often neglected due to high dielectric constant of semiconductor material). According to a prediction made by L. Irimpan, the band gap of ZnO nanocrystals ranges from 3.5 to 4 eV in the range of 4.5 to 18 nm in particle size.

A physical scenario of propagating wave through crystal lattice with lattice constant a can be described by Bragg refection. Bragg condition in lattice environment satisfied.

$$k +)^2 = k^2 \qquad (28)$$

The wave numbers k_1, k_2 differing by a value

$$k_1 - k_2 = 2\pi n/a \qquad (29)$$

where n=±1, ±2, ±3…….

Hence the magnitude of k values contain the intervals $-\pi/a < k < +\pi/$, $\pi/a < k < +3\pi/a$, $3\pi/a < k < +5\pi/a$,…………

Width of the Brillouin zone is $2\pi/a$ each. In this type periodic potential dispersion curve has discontinuities at point

$$kn = \pi n/a \quad \text{where n=±1, ±2, ±3} \qquad (30)$$

At this value of k the propagating wave function results in standing wave that leads to multiple reflection from periodic structure. At each value of kn two standing waves exist with different potential energy values. The difference in energy values between the standing waves is responsible for an energy gap. For two consecutive values of n a forbidden energy interval exists where no propagating wave exist. Typically different zone exist in k space between $-\pi/a < k < +\pi/a$, $-2\pi/a < k < +2\pi/$, …. and so on. So the energy spectra dispersion curve has discontinuities at

$$kn = \pi n/a, \text{ where n= ±1, ±2, ±3 ..} \qquad (31)$$

Standing waves for different n values arise multiple reflections from the periodic structure. The region in k space between $-\pi/a$ and $+\pi/a$ is called the first Brillouin zone (BZ). The different parabolic branch may folded back into first Brillouin zone as depicted in Figure.17.
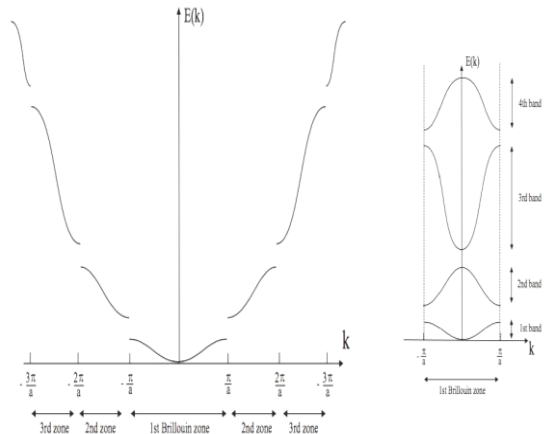

Figure.17: (a) The E versus K diagram showing 2π displacements of several sections of allowed energy bands. (b) The E versus K diagram in the reduced-zone representation.

Bragg reflection at $k=\pm\pi/$ produces standing waves. Probability The average potential energy should be lower than for a freely moving wave due to the distribution of electron density in periodic potential, which is either concentrated at positive ion cores or distributed across ion cores and resulting in an increase in potential energy. The energy gap in crystals is caused by the energy difference between the standing waves. In the region of energy space known as the bandgap, the greatest occupied energy level in the conduction band (CB) and the lowest unoccupied energy level in the valence band (VB) are energetically separated by the bandgap energy Eg. An electron from VB to CB is excited over a certain threshold frequency, leaving a hole in the VB in its wake. The bandgap energy may be probed by absorption spectroscopy.

VI. EFFECTIVE MASS OF ELECTRONS AND HOLES

Electrons and holes are quasi-particles associated with quasi-momentum. The typical value of quasi-momentum is governed by

$$p = \hbar k = 2\pi\hbar/a \qquad (32)$$

Equation (32) has direct consequence of translation symmetry of periodic lattice. Although for free particle one can formulate the energy values in k space as

$$(k) = h^2 k^2/2m^*(k) \qquad (33)$$

Where m^* is referred as effective mass. In case of each periodic potential there exist extrema in band structure. At center of Brillioun zone of a given extremum $E_0(k_0)$ can be written as

$$(k) = E_0 + (k-k_0) [dE/dK] \big| k=k_0 + 1/2 (k-k_0)^2 [d^2E/dk^2] \big| k=k_0 + \qquad (34)$$

If it is considered that the energy is measured from E_0 i.e $E_0=0$, and the wavenumber is measured from k_0 that is $k_0=0$ then at extrimum $[d(k)/dK]=0$

$$(k)=0.5k^2 \{ d^2E/dk^2 \} \big| k=0+ \qquad (35)$$

By neglecting higher order terms of k for near extremunm point from equation (34)

$$m*^{-1}=(1/\hbar^2) \{d^2E/dk^2\} \big| k=0=const. \qquad (36)$$

Omitted terms of higher order than $k2$ corresponds to the parabolic band of crystals. Equation (36) determines the electron effective mass. At $k = 0$ it can be taken as constant. Usually it is given as units of the vacuum electron mass me.

VII. QUASIPARTICLES: ELECTRON, HOLE AND EXCITON

When an electron in the conduction band undergoes primary elementary excitation by the absorption of energy over the bandgap, a nearby elementary quasiparticle hole is also generated. Using the idea of elementary excitation, we may think of the ground state of a crystal as a vacuuming condition, where neither an electron nor a hole are present, and the first excited state, where an electron and a hole are present in the conduction band and valence band, respectively. When a perturbation is applied, a transition is conceivable. The perturbed photonic absorption by the crystal lattice maintains energy momentum conservation.

$$\hbar\omega=E_g+E_{e\ kin}+E_{h\ kin} \qquad (37)$$

$$\hbar k=\hbar k_e+\hbar k_h \qquad (38)$$

As a result, the photon momentum is very minimal only because a vertical transition occurs. The opposite process, which is known as a downward radiative transition, is likewise capable of annihilating an e-h pair and producing a photon. Under an elementaryly excited environment, electrons and holes interact through Coulomb potential interaction to create an additional quasiparticle known as an exciton, which corresponds to the electron-hole pair's bound state that resembles hydrogen. A Hamiltonian may be used to describe the electron hole and exciton interaction in the current circumstance.

$$H=-\{\hbar^2/2m*_e\}\nabla_e^2-\{\hbar^2 / 2m*_h\nabla_h^2 \} -$$
$$\{e^2/[4\pi\varepsilon_0\varepsilon \big| r_e-r_h \big| \} \qquad (39)$$

Which is the same Hamiltonian of hydrogen atom with masses $m*_e$ and $m*_h$ instead of m_0 and M and ε is the dielectric constant of crystal. Hence similar to the hydrogen atom , exciton is characterized by the exciton Bohr radius as

$$a_{ex}= \{4\pi\varepsilon0\varepsilon\hbar^2 / \mu e^2 \} \qquad (40)$$

Where μ is the reduced mass of electron-hole pair $1/\mu=1/m_h*+1/m_e*$. Absolute value of Bohr excition radius for the common semiconductors in the range of few nanometer. Thus the excition is delocalized over several thousands of atoms in the lattice.

VIII. QUANTIZATION OF ENERGY STATES IN SEMICONDUCTOR NANOCRYSTALS

In general, the de Broglie wavelength and exciton Bohr radius of quasiparticles are longer than the lattice constant of the majority of conventional semiconductors. Given the abundance of atoms in crystallites, they may be regarded as macroscopic systems in terms of lattice characteristics. It should be remembered that quasiparticles are tied to an endless three-dimensional potential well on the path to nanocrystal creation. The energy of an exciton for quantization as follows

$$E_{l,e\cdot h}=\hbar^2\Phi_{l,n}^2/2m_e,h*R^2 \qquad (41)$$

Where $m_e,h*$ is the effective mass of electrons and holes , R is the radius of nanocrystal. $\Phi_{l,n}$ is the nth root of the spherical Bessel function. From equation (41) we can say size reduction of nanocrystals leads to energy difference enhancement between consecutive states. This event results in blue shifting of bandgap absorption edge.

IX. MOSS-BURSTEIN EFFECT

The carrier concentration in excess of critical Mott carrier density36 by doping in semiconductor nannocrystal often results in a widening of the intrinsic optical band gap *(Eg),* is well known Burstein-Moss shift37 (Figure.18.). The Fermi energy (EF), which is present in the conduction band due to substantial n-type doping, is thought to be responsible for this phenomena (or in the valence band for p-type doping). This limits thermal or optical stimulation in the filled states. As a result, the band gap measured from the beginning of interband absorption increases (i.e. suffers "a blue shift"). The magnitude of the shift (*EΔBM*), under free-electron theory, prescribed as

$$\Delta E_{BM}=\hbar^2/2m* \{ (3\pi^2n_e)\}^{2/3} \qquad (42)$$

Where $m*$ is the is the exciton pair reduced effective mass (μ) as $1/\mu=1/m_h*+1/m_e*$ and n_e is the carrier concentration.
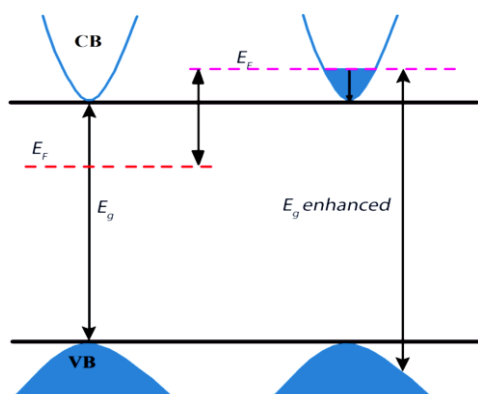

Figure.19. Bandgap (E_g) enhanced due to B-M.

X. ELECTRICAL PROPERTIES

Degenerately conduction band filling in semiconductor nanocrystals by aliovalent doping or vacancy doping enhance the carrier concentration. Typically when the carrier concentration exceeds Mott's critical density nc metallic conduction behavior arises in material. At ambient temperature, a highly doped semiconductor thin sheet exhibits metallic conductivity, and at low temperatures, a metal to semiconductor transition (MST) occurs. Due to the localization of carriers caused by disorder, which hampered the thin film's ability to transport metallic materials, semiconducting behaviour at low temperatures was seen in as-deposited thin films. This means that high carrier concentration, which is statistically occupied at lattice or interstitial sites, is caused by both aliovalent dopants and native point defects. In order to localise the delocalized degenerate electronic states at Fermi level, these defective states induce lattice disorders. In a degenerate semiconductor, the MST transition results from the prevalent presence of metallic conductance caused by the Mott criteria and Anderson localization caused by disorder. By employing back scattering in the semiconducting area and phonon-like scattering in the metallic region, it is possible to study MST-like transition.

MST like transport feature can be fitted by following equation:

$$(t) = \{1/[a_0+a_1T^{p/2}+a_2T^{1/2}]\}+bT^2 \tag{43}$$

Where a_0 is related to the residual resistivity $\rho0$ ($a_0=1/\rho0$), $a_1T^{p/2}$ p depends on the kind of interactions

and p = 2 or 3 characterises the weak localization caused by the self interference of quantum wave functions backscattered on impurities. $a_2T^{1/2}$ refers to the Coulomb electron interactions that have been renormalized by self-interference effects, and explains the weak localization caused by the self interference of quantum wave functions backscattered on impurities, where p depends on the nature of the interactions. In fact, in these modifications, a component called bT2 is included to account for the effect of high temperature scattering. It has to be noticed that without quantum corrections $a_1 = a_2 = 0$, this expression reduces to the Boltzmann formulas.

XI. BASIC PRINCIPLES OF SEMICONDUCTOR PHOTOCATALYSIS

The function of a photocatalyst is to start or speed up a certain redox process (reduction and oxidation) in the presence of light energy in order to obtain promising results in photochemistry. When photons with energies larger than or equal to the bandgap are used to light the photocatalyst, one electron (ecb-) is transferred from the valance band to the conduction band, leaving a hole (hvb+), as shown in Figure 20. In fact, the excited electron and hole travelled to the semiconductor's surface. While holes in the VB should have a chemical potential energy of +1.0 to 3.5 V vs in NHE demonstrate significant oxidative potential, excited electrons should have a chemical potential energy of +0.5 to -1.5 V versus in normal hydrogen electrode (NHE) scale. In order to react with the electron donors (D) and electron acceptors (A) adsorbed on the surfaces of the semiconductor nanocrystals, excited ecb- and hvb+ may operate as a reductant and an oxidant, respectively.
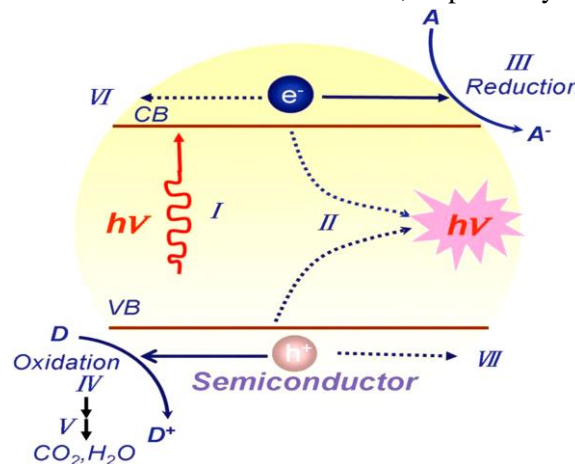
Figure.20: Schematic representation of how semiconductor photocatalysis works: (I) a photon forms charge carriers; (II) charge carriers recombinate to release heat; (III) a conduction-band electron initiates a reductive pathway; (IV) a valence-band hole initiates an oxidative pathway; (V) additional thermal (such as hydrolysis or a reaction with active oxygen species) and photocatalytic reactions yield mineralization products; and (VI).

The next step should be the excited state conduction-band electrons and valance band holes can recombine and loss its exited energy if the recombination is perturbed by scavengers or by crystalline defects then minimization of recombination results in increased efficiency in the usage of the photogenerated carriers for desired photoreaction. Indeed it is clear that only energetic enough electors and holes can reach the surface of semiconductor without recombination can stimulate the redox reaction. It is essential for successful surface reaction that the reduction and oxidation potential are more positive and negative than CB and VB level respectively as some standard redox reaction is given in Table .1.

Table.1. Standard redox potentials for some typical species:

Reaction	$E^0(V)$ vs NHE at pH 0
$2H^+ + 2e^- \rightarrow H_2(g)$	0
$O_2(g) + e^- \rightarrow O_2^-(aq)$	−0.33
$O_2(g) + H^+ + e^- \rightarrow HO_2^\bullet(aq)$	−0.046
$O_2(g) + 2H^+ + 2e^- \rightarrow H_2O_2(aq)$	0.695
$2H_2O(aq) + 4h^+ \rightarrow O_2(g) + 4H^+$	1.229
$OH^- + h^+ \rightarrow \bullet OH$	2.69
$O_3(g) + 2H^+ + 2e^- \rightarrow O_2(g) + H_2O$	2.075
$CO_2 + e^- \rightarrow CO_2^-$	−1.9
$2CO_2(g) + 2H^+ + 2e^- \rightarrow HOOCCOOH(aq)$	−0.481
$CO_2(g) + 2H^+ + 2e^- \rightarrow HCOOH(aq)$	−0.199
$CO_2(g) + 2H^+ + 2e^- \rightarrow CO(g) + H_2O$	−0.11
$CO_2(g) + 4H^+ + 4e^- \rightarrow C(s) + 2H_2O$	0.206
$CO_2(g) + 4H^+ + 4e^- \rightarrow HCHO(aq) + H_2O$	−0.07
$CO_2(g) + 6H^+ + 6e^- \rightarrow CH_3OH(aq) + H_2O$	0.03
$CO_2(g) + 8H^+ + 8e^- \rightarrow CH_4(g) + 2H_2O$	0.169
$2CO_2(g) + 8H_2O + 12e^- \rightarrow C_2H_4(g) + 12OH^-$	0.07
$2CO_2(g) + 9H_2O + 12e^- \rightarrow C_2H_5OH(aq) + 12OH^-$	0.08
$3CO_2(g) + 13H_2O + 18e^- \rightarrow C_3H_7OH(aq) + 18OH^-$	0.09
$H_2O_2(aq) + H^+ + e^- \rightarrow H_2O + OH^-$	1.14
$HO_2^\bullet + H^+ + e^- \rightarrow H_2O_2(aq)$	1.44
$H_2O_2(aq) + 2H^+ + 2e^- \rightarrow 2H_2O$	1.763

XII. FUNDAMENTALS OF WATER SPLITTING

The basics fundamental of water splitting as follows : The water molecule are reduced to from H_2 and oxidized to form O_2. The reduction and oxidation are mediated by electrons and holes, respectively. The redox potential of water is 1.23 V, i.e. H+/H2 is 0 V and O2/H2O is 1.23 V with respect to the normal hydrogen electrode (NHE).

Essential knowledge about CB and VB band energy level of semiconductor with respect to redox potential of H2O i.e. the CB edge should lower than the H2/H+ potential (0 V vs. NHE) and VB edge should be higher than O2/OH− (1.23 V vs. NHE) potential) is essential to meet the success in H2 production (Figure.21).
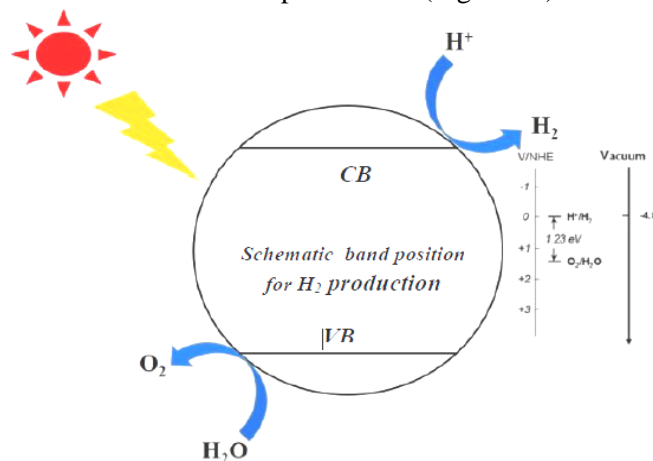

Figure.21: Bandgap position in NHE scale.

XIII. CONCLUSION

The most important outcome of the research results presented in the paper is an enhancement of photophysical properties of wide bandgap nanoscale semiconductors: Firstly, electronic and optical properties are modified by synthesizing semiconductor nanocrystals to introduce quantum confinement effect i.e. increase of band gap with reduction of size. The research work presented here, on preparation of nano scale semiconductor by colloidal synthesis and characterization of these samples by optical and electrical studies. Photophysical properties of nanocomposite are also studied like H2 generation from water, pollutant dye degradation and carcinogenic Cr(VI) reduction from water under irradiation of solar simulator light. In following section a brief outline of optical and electrical properties in nano scale semiconductors are discussed.

XIV. REFERENCES

1. W. Xie, B. Liu, S. Xiao, H. Li, Y. Wang, D. Cai, D. Wang, L. Wang, Y. Liu, Q. Li, T. Wang, *Sensors and Actuators B* 2015, 215, 125–132.
2. V. C. Sunder, H. J. Eister, T. Deng, Y. Chan, E. L. Tomas, M. G. Bawendi, Adv. Mater. 2004,16,2137-2141. (17) Y-W. Jun, J-H. Lee, J
3. N. Parveen, S. A. Ansari, H. R. Alamri, M. O. Ansari, Z. Khan, M. H. Cho, *ACS Omega* 2018, 3, 1581−1588.

4. M. Nasilowski, B. Mahler, E. Lhuillier, S. Ithurria, B. Dubertret, *Chem. Rev*. 2016, 116, 10934−10982.

5. X. Peng, L. Manna, W. Yang, J. Wickham, E. Scher, A. Kadavanich, A. Alivatos, *Nature* 2000,404,59-61.

6. D. J. Milliron, S. M. Hughes, Y. Cui, L. Manna, J. Li, L.W. Wang, A. P. Alivisatos, *Nature* 2004, 430, 190-195.

7. J. Borges, A. J. Ribeiro, M. E. Pereira, A. C. Carreira, M. C. Pereira, F. Silva, *J. Colloid Interface Sci.* 2011, 358, 626.

8. N. Wetchakun, S. Chaiwichain, B. Inceesungvorn, K. Pingmuang, S. Phanichphant, A. I. Minett, J. Chen, *ACS Appl. Mater. Interfaces,* 2012, 4,3718.

9. L. Y. Huang, H. Xu, Y. P. Li, H. M. Li, X. N. Cheng, J. X. Xia, Y. G. Xu, G.B. Cai, *Dalton. Trans*.2013, 42, 8606.

10. J. G. Yu, S. H. Wang, J. X. Low, W. Xiao, *Phys. Chem. Chem. Phys*.2013, *15*, 16883.

11. L. Novotny and B. Hecht, *Principles of nano-optics*. Cambridge university press, 2012.

12. D. R. Smith, J. B. Pendry, and M. C. K. Wiltshire, "Metamaterials and negative refractive index," *Sci.*, vol. 305, no. 5685, pp. 788–792, 2004.

13. E. Hutter, J. H. Fendler, *Adv. Mater.* 2004, 16, 1685-1706

14. W.A. Murray ,W. L. Barnes *Adv. Mater*.2007, 19,3771-3782.

15. M. Sturaro, E. D. Gaspera, N. Michieli, C. Cantalini, S. M. Emamjomeh, M. Guglielmi, A. Martucci, *ACS Appl. Mater. Interfaces*,2016, *8*, 30440–30448.

16. M. Xi, B. M. Reinbard, *J. Phys. Chem. C* 2018, 122, 5698−5704.

17. S. Ghosh, M. Saha, S. K. De, *Nanoscale* 2014, 6, 7039-7051.

18. Agarwal, S. H. Cho, O. Zandi, S. Ghosh, R. W. Johns, D. J. Miliron, *Chem. Rev.* 2018, 118, 3121−3207.

19. G. V. Naik, V. M. Shalaev, A. Boltasseva, *Adv. Mater.* 2013, 25, 3264-3294.

20. Kriegel, C. Jiang, J. R.-Fernandez, R. D. Schaller, D. V. Talapin, E. da. Como, J. Feldmann, *J. Am. Chem. Soc*. 2012, 134, 1583-1590.

21. M. Luther, P. K. Jain, T. Ewers, A. P. Alivisatos, *Nature Mater.* 2011, 10, 361-366.

22. D. Dorfs, T. Hartling, K. Mistaza, N. C. Bigall, M. R. Kim, A. Genovese, A. Falqui, M. Povia, L. Manna, *J. Am. Chem. Soc*. 2011, 133, 11175-11180.

23. V. B. Llorente, V. M. Dzhagan, N. Gaponik, R, A. Iglesias, D. R. T. Zahn, V. Lesnyak, *J. Phys. Chem. C* 2017, 121, 18244−18253.

24. Callegari, D. Tonti, M. Chergui, *Nano Lett*., 2003, 3,1565-1568.

25. E. D. Gaspera, M. Bersani, M. Cittadini, M. Guglielmi, D. Pagani, R. Noriega, S. Mehera, A. Salleo, A. Martucci, *J. Am. Chem. Soc.* 2013, 135, 3439−3448.

26. S. Ghosh, M. Saha, V. D. Ashok, B. Dalal, S. K. De, *J. Phys. Chem. C* 2015,*119*, 1180–1187.

27. U. Kreibig, M. Vollmer, *Optical Properties of Metal Clusters*, Springer, 2010.

28. S. Hunklinger, *Festkörperphysik*, Oldenbourg Wissensch.Vlg, 2009.

29. Kriegel, F. Scotognella, L. Manna, *Physics Reports* 2017,67, 1–52.

30. N.W. Ashcroft and N.D. Mermin.Solid state Physics.Saunders College, Philadelphia, PA 19105, *hwr international edition*, 1976.

31. C.F. Bohren and D.R. Huffman.Absorption and scattering of light by small particles Wiley science paperback series. John Wiley & Sons, Inc., New York, 1983.

32. T. Okamoto.Near-field optics and surface plasmon polaritons, volume 81 of Topics in Applied Physics . Pages 97-122, Springer, 2001.

33. S. Link, M. A. El-Sayed, *J. Phys. Chem. B* 1999, 103, 4212-4217.

34. Mie, G., Beiträge zur optik trüber medien, speziell kolloidaler metallösungen. *Ann. Phys.* 1908, 330, 377-445.

35. G. C. Papavassiliou, *Prog. Solid State Chem.* 1980, *12*, 185.

36. M. Luther, P. K. Jain, T. Ewers and A. P. Alivisatos, Nat. Mater., 2011, 10, 361–366 .

37. S. D. Lounis, E. L. Runnerstrom. A. Bergerud, D. Nordlund, D. J. Milliron, *J. Am. Chem. Soc.*, 2014, 136, 7110–7116.

38. S. Link, M. B. Mohamed , M. A. El-Sayed *J. Phys. Chem. B* 1999, 103, 3073-3077.

39. R. Gans, Über die Form ultramikroskopischer Goldteilchen. *Annalen der Physik,*1912, 342, 881-900.

40. S. Link, M. A. El-Sayed, *J. Phys. Chem. B* 1999, 103, 8410-8426.

41. T. Edvinsson R. Soc. open sci. 5: 180387.

42. E. Brus, *Journal of Chemical Physics*,1984,80, 4403.

43. Irimpan, V. P. N. Nampoori, P. Radhakrishnan, *J. Appl. Phys.* 2008, 104, 033118.

44. L Efros, M. Rosen, *Annual Review of Materials Science* 2000, 30, 475-521.

45. F. Mott, Philos. Mag. 6, 287 ,1961.

46. E. Burstein, Phys. Rev. 93, 632 ,1954.

47. F. Mott, Conduction in Non-Crystalline Materials, Clarendon Press,Oxford, 1993

48. M. Nistor, F. Gherendi, N. B. Mandache, C. Hebert, J. Perrière, W. Seiler, *J. Appl. Phys.* 2009, 106, 103710.

49. D. Saha, A.K. Das, A. P. Misra, L. M. Kukreja, *J. Appl. Phys.* 2013, 114, 043703.

50. H.Wang, L. Zhang, Z. Chen, J. Hu, S. Li, Z. Wang, J. Liu, X. Wang, *Chem. Soc. Rev.,* 2014, 43, 5234-5244.

51. Wen, J. Xie, X. Chen, X. Li, *Applied Surface Science* 2017, 391, 72–123

52. V. J. Babu, S. Vempati, T. Uyar, S. Ramakrishna *Phys. Chem. Chem. Phys.,* 2015, 17, 2960-2986.

Cite this article as :